Short Papers

3D Fingerprint Recognition based on Ridge-Valley-Guided 3D Reconstruction and 3D Topology Polymer Feature Extraction

Xuefei Yin, Yanming Zhu, and Jiankun Hu, *Senior Member, IEEE*

Abstract—An automated fingerprint recognition system (AFRS) for 3D fingerprints is essential and highly promising for biometric security. Despite the progress in developing 3D AFRSs, achieving high-quality real-time reconstruction and high-accuracy recognition of 3D fingerprints remain two challenging issues. To address them, we propose a robust 3D AFRS based on ridge-valley (RV)-guided 3D fingerprint reconstruction and 3D topology polymer (TTP) feature extraction. The former considers the unique fingerprint characteristics of the RV and achieves real-time reconstruction. Unlike traditional triangulation-based methods that establish correspondences between points by cross-correlation-based searching, we propose to establish RV correspondences (RVCs) between ridges/valleys by defining and calculating a RVC matrix based on the topology of RV curves. To enhance depth reconstruction, curve-based smoothing is proposed to refine our novel RV disparity map. The TTP feature codes the 3D topology by projecting the 3D minutiae onto multiple planes and extracting their corresponding 2D topologies and has proven to be effective and efficient for 3D fingerprint recognition. Comprehensive experimental results demonstrate that our method outperforms the state-of-the-art methods in terms of both reconstruction and recognition accuracy. Also, due to its very short running time, it is appropriate for practical applications.

Index Terms—Biometrics, 3D fingerprint recognition, real-time 3D fingerprint reconstruction, 3D topology feature extraction

1 Introduction

As one of the most reliable and discriminative biometrics, a fingerprint has been widely used in various applications, such as personal electronic products, secure payments, forensics and security [1]. Its dominance has been established by the continuous emergence of various automated fingerprint recognition systems (AFRSs), with current ones focusing mainly on two-dimensional (2D) contact fingerprints, the acquisition of which requires physical contact between the fingers and sensor's surface. Although 2D contact fingerprints are easy to obtain and usually have high ridge-valley (RV) contrasts, the process for capturing them tends to simultaneously introduce inconsistencies and distortions through physical contact, which thereby affects an AFRS's accuracy [2]. Also, interference caused by the latent fingerprints left on a scanner platen easily leads to issues of contaminated fingerprints, failed acquisitions, and poor hygiene. More importantly, 2D fingerprints cannot truly represent natural three-dimensional (3D) ones because they lose 3D information during acquisition when a curved 3D finger is flattened against a 2D plane. Therefore, AFRSs for 3D fingerprints have been proposed in recent yeas [3], [4], [5], [6], [7], [8], [9], [10], [11], [12], [13].

- *The authors are with the School of Engineering and Information Technology, University of New South Wales, CanberraACT2600, Australia. E-mail: {xuefei.yin, yanming.zhu}@student.unsw.edu.au, J.Hu@adfa.edu.au.*

Manuscript received 11 Feb. 2019; revised 14 Oct. 2019; accepted 15 Oct. 2019. Date of publication 30 Oct. 2019; date of current version 3 Feb. 2021.
(Corresponding author: Jiankun Hu.)
Recommended for acceptance by J. Zhou.
Digital Object Identifier no. 10.1109/TPAMI.2019.2949299

1.1 Motivation and Previous Studies

Despite progress in the development of 3D AFRSs, the two critical problems still needing to be solved are: how to reconstruct accurate 3D fingerprints in real time; and how to extract effective 3D fingerprint features and compare them. This paper aims to address these two issues and achieve a robust 3D AFRS.

1.1.1 3D Fingerprint Reconstruction

In recent years, several methods proposed for 3D fingerprint reconstruction can be classified into three main categories based on their imaging techniques: 1) photometric stereo [3], [4], [5], [6]; 2) structured light scanning [7], [8], [9], [10]; and 3) stereo vision [11], [12], [13].

Photometric stereo-based reconstruction requires capturing multiple 2D fingerprint images under different illuminations using a fixed high-speed camera. Its underlying principle is that 3D surface reflectance can be determined by its orientation with respect to the light source and observer [14], with the methods in [3], [4], [6] and [5] reconstructing 3D fingerprint information by estimating the surface normal. However, although their hardware systems are relatively low-cost and compact (consisting of a high-speed camera and several LEDs), they are extremely time-consuming due to the expense of computing the surface normal for each pixel; for example, it takes approximately 180 seconds to reconstruct a 3D fingerprint with a resolution of 300×200 in [4]. Moreover, they require a large random-access memory to store the pre-calibrated data [5], [6].

Reconstructing 3D fingerprints based on structured light scanning requires capturing multiple 2D fingerprint images with projected patterns using several high-speed cameras and a DLP projector. Its principle is triangulation, whereby the 3D depth information is recovered according to the correspondences between images. As, in methods [7], [10] and [8], the correspondences between the points of observed and projected patterns are precisely pre-encoded, 3D fingerprints are reconstructed by measuring the deformations of the projected patterns. The advantage of this type of method is that RV details can be recovered and relatively accurate 3D depth information generated. However, their hardware systems are very expensive and bulky due to the special projector and high-speed cameras they require.

Reconstructing 3D fingerprints based on stereo vision requires capturing different views of 2D fingerprint images using two or more cameras and then calculates the 3D depth information between corresponding points according to the triangulation principle. However, although the advantages of this type of method are that it is simple, low-cost and relatively compact, current ones rely greatly on establishing correspondences between points which is computationally complex and time-consuming. For example, the state-of-the-art methods in [12] and [13] still take 1.5 minutes to reconstruct one 3D fingerprint which is unsuitable for practical applications and, more importantly, fail to recover RV details since the correspondences they established are based on block regions rather than pixels.

Recently, several ones based on optical coherence tomography and ultrasonic imaging have been proposed. The former methods are accurate and have a potential anti-spoofing capability but are very expensive [15], [16], [17], [18], at least $7000 according to the report in [19]. The latter methods are low-cost but time-consuming [20], [21], [22], for example, it takes approximately 5 seconds to reconstruct a 3D fingerprint with a resolution of 1000 dpi in [22]. Also, this type of method is not completely contactless since it requires fingers to be pressed against a platen during acquisition.

Therefore, in this paper, we propose a novel RV-guided 3D fingerprint reconstruction method which is robust and can achieve highly accurate 3D reconstruction in real time.

1.1.2 3D Fingerprint Feature

In the recent decades, only a few 3D fingerprint features has been developed for recognizing 3D fingerprints. Liu et al. [23] proposed one based on the surface curvature of a 3D fingerprint, which contains information of the overall structure of the fingerprint and indicates the distribution of other features. However, it is not effective and has poor recognition accuracy (equal-error rates (EERs) of 15 and 14.4 percent, respectively) according to [23] and [6]. Kumar et al. [5] proposed a 3D minutia feature denoted as a 5-tuple composed of three coordinates and two ridge orientations in 3D space. However, using this feature to achieve a 3D fingerprint comparison is computationally expensive and time-consuming. To reduce computational complexity, Lin et al. [6] proposed a Delaunay tetrahedron-based 3D minutia feature defined as a convex polyhedron consisting of four triangular faces of 3D minutiae but its spatial topology is susceptible to spurious and missing 3D minutiae [24], [25]. Therefore, implementing an effective 3D fingerprint feature is urgent. Inspired by the success of 2D local minutiae structures in [1], [26], [27], [28], [29], [30], [31], in this paper, we propose a novel 3D topology polymer (TTP) feature that achieves highly accurate 3D fingerprint recognition.

1.2 Our Work and Contributions

We achieve a robust 3D AFRS based on RV-guided 3D fingerprint reconstruction and TTP feature extraction. The former is based on the topology of RV curves, whereby successful RV details and well-structured 3D surfaces can be achieved by establishing a RV correspondence (RVC) between different views of fingerprint images. In it, different views of fingerprint images are first pre-processed to generate severed RV maps (SRVMs) (see details in Section 2.2), based on which a RVC matrix (RVCM) is defined to measure the degree of correspondence between RVs and calculated by our proposed dynamic algorithm in one-dimensional (1D) space. Then, the RVC is established according to the RVCM by our proposed greedy algorithm. Finally, a novel RV disparity map (RDP), which adopts curve-based smoothing to separately refine the disparities of ridges and valleys, is calculated to reconstruct the 3D depth. Based on this reconstructed 3D fingerprint, a TTP feature is extracted for 3D fingerprint recognition as follows. First, 3D minutiae are extracted and re-represented in multiple new 3D spaces and then by projecting them onto multiple planes and coding their corresponding 2D topologies, the TTP is extracted. Comprehensive experimental results demonstrate that the proposed method outperforms state-of-the-art ones in terms of both reconstructing and recognition a 3D fingerprint.

The key contributions of our work are summarized as follows.

1) Traditional methods for 3D fingerprint reconstruction usually establish correspondences based on points, which are particularly time-consuming and fail to recover RV details. In this paper, we propose a RVC based on the topology of RV curves, which fully considers the unique fingerprint characteristics of the RVs and can reduce computational complexity. In comparison with traditional methods, it achieves successful 3D fingerprint RV reconstruction and generates well-structured 3D surfaces.
2) Unlike conventional methods that establish correspondences using cross-correlation-based searching, we propose achieving this by defining and calculating a RVCM. To the best of our knowledge, this is the first of this type of approach and more importantly, this RVCM is defined on RV curves and calculated in 1D, rather than the traditional 2D, space, which significantly improves the efficiency of establishing correspondences.
3) We propose a RDP for reconstructing 3D depth information and a curve-based smoothing to refine the RDP. Unlike traditional methods that calculate disparity based on pixels in a 2D space and tend to damage a RV's depth structure, our proposed RDP is based on RVs and, as it performs smoothing in 1D space separately for ridges and valleys, it ensures effectiveness and reduces computational complexity.
4) We propose a robust TTP feature which fully exploits 3D topological information of 3D minutiae. By projecting 3D minutiae onto multiple planes and coding their corresponding 2D topologies, this feature is efficiently extracted with finite dimensions, and the experiments demonstrate its effectiveness.
5) To the best of our knowledge, this is the first method that achieves real-time 3D reconstruction (less than 0.1 seconds to reconstruct 1M points). Also, the proposed TTP feature significantly improves the speed of 3D fingerprint recognition by approximately 16 times that of the state-of-the-art method in [6].

The rest of this paper is organized as follows: Section 2 describes the proposed RV-guided 3D fingerprint reconstruction method in detail; Section 3 presents the proposed 3D fingerprint TTP feature and the recognition; the experiments and results are provided and discussed in Section 4; and, finally, the paper is concluded in Section 5.

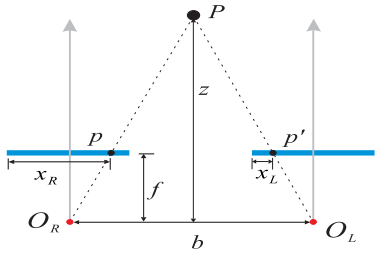

Fig. 1. Diagram of basic principle of triangulation, where P is a point of a 3D object, p and p' its corresponding points in 2D images captured by two cameras, O_R and O_L the centers of the left and right cameras, respectively, f the distance between the lens and image plane, b the distance between the centers of the two camera centers, and $x_R - x_L$ the disparity of point p in the left image.

2 RV-Guided 3D Reconstruction

The proposed RV-guided 3D fingerprint reconstruction method is based on the classical triangulation principle [32] which is illustrated in Fig. 1. Given two rectified images (left and right) of the same scene, the depth $z(x, y)$ of point (x, y) in the left image is calculated by

$$z(x, y) = b * f/d(x, y), \tag{1}$$

where $d(x, y)$ is the disparity of (x, y), b the distance between the centers of two cameras, and f the focal length of the camera. Assuming that point (x', y) in the right image corresponds to point (x, y) in the left one, the disparity $d(x, y)$ is defined as the number of pixels between these two points and calculated by

$$d(x, y) = x - x'. \tag{2}$$

It is easy to determine that the key to reconstructing a 3D fingerprint is establishing correspondence. Unlike traditional methods for achieving this, we propose a RV-guided one which fully exploits the unique characteristics of a 3D fingerprint and is both effective and efficient (Section 2.3).

2.1 Camera Calibration

Camera calibration, which estimates a camera's intrinsic parameters and extrinsic ones, is a fundamental step in 3D reconstruction. We use a three-camera system calibrated off-line based on the methods in [32], [33], [34], [35]. The middle camera is selected as the reference,

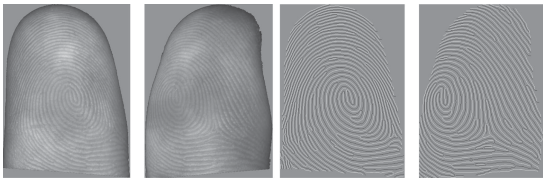

Fig. 2. A pair of rectified 2D fingerprint images (a) the middle-view image and (b) the right-view image and their respective SRVMs (c) and (d), with white curves refer to ridges and dark curves refer to valleys.

with its experimental implementation achieved using the toolboxes in [36] and [37]. The accuracy of camera calibration is generally estimated by the re-projection error [33], the mean of which in our calibration is approximately 0.4305 pixels or 0.0110 mm.

2.2 Pre-Processing of Fingerprint Images

To facilitate the establishment of correspondence, we pre-process 2D fingerprint images in the following four steps: 1) extract their fingertip regions using a pre-trained convolutional neural network (CNN) which is similar to the one in [38] but replaces the training database; 2) rectify the extracted images using the parameters of the calibrated camera so that corresponding points have the same row coordinate and the establishing of 2D correspondence is reduced to a 1D space which greatly decreases computational complexity; 3) first binarize the rectified images using a fast implementation of the STFT method [39] and then thin the binary image and its complement, respectively, to form a RV map; and 4) generate a SRVM by removing the bifurcation minutiae points and their 8-connected neighborhoods in the RV map so that all the ridges and valleys are split into isolated curves to provide the basis for RVC establishment and then mathematically update the SRVM by assigning different positive and negative integer values to different ridge and valley curves, respectively, with the same curves having the same values and zero referring to the background. Fig. 2 shows an example of a pair of rectified images and their SRVMs.

2.3 Establishment of RVC

The proposed establishment of RVC is based on an obvious proposition: if two ridges/valleys in the rectified stereo fingerprint images correspond, so do their proximate valleys/ridges. This is easy to understand because, as the corresponding points in 3D space will be projected onto the same row in two 2D images, the topological relationship between the ridges and valleys will be well preserved and able to be used as a guide to establish correspondence.

To establish the RVC, first, a RVCM is defined based on the SRVM to record the degree of correspondence between their RVs (Section 2.3.1). Then, a dynamic algorithm calculating the RVCM (Section 2.3.2) and a greedy algorithm establishing the RVC (Section 2.3.3) are developed.

2.3.1 Definition of RVCM

Assuming that $\mathcal{M}$ and $\mathcal{M}'$ are two SRVMs of different views of two fingerprint images, where $\mathcal{M}$ contains n_r isolated ridge curves and n_v isolated valley curves, and $\mathcal{M}'$ contains n'_r isolated ridge curves and n'_v isolated valley curves, then the RVCM M is defined as a $(n_r + n_v) \times (n'_r + n'_v)$ matrix in which element e_{ij} is a weight that measures the degree of correspondence between ridges/valleys i and j in $\mathcal{M}$ and $\mathcal{M}'$, respectively, with a larger value indicating a better correspondence. The initial values of M are zeros and its calculation is detailed in Section 2.3.2.

2.3.2 Calculation of RVCM

The RVCM is calculated by matching the RV curves according to the SRVMs. To reduce computational complexity and improve accuracy,

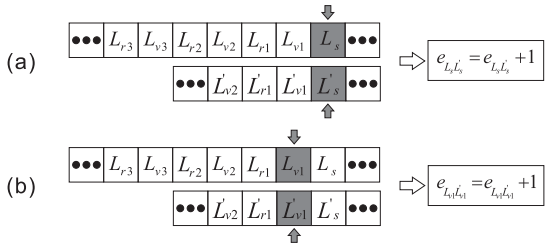

Fig. 3. Diagram of proposed *Row-Operator* calculating M backwards from (a) matched pair of labels L_s and L'_s to (b) previous pair of valley curve labels L_{v1} and L'_{v1}.

a benchmark pair of curves is determined by selecting a benchmark pair of minutiae which leads to the maximum number of minutia matches when used as the reference one. In our work, minutiae are extracted from ridge map according to the Standard ANSI/NIST-ITL 1-2007. Unlike traditional methods that use each pair of minutiae as reference one, we constrain this selection by $x - x' > 0, |y - y'| < \sigma_y, t == t'$, and $l > \sigma_l \ \ and \ \ l' > \sigma_l$, where (x, y) and (x', y') are the coordinates of minutiae $\mathbf{m} = \{x, y, \theta, t\}$ and $\mathbf{m}' = \{x', y', \theta', t'\}$, respectively, t and t' the types of minutia, l and l' the lengths of the curves where minutiae $\mathbf{m}$ and $\mathbf{m}'$ are located, and σ_y and σ_l the thresholds. The constraint term $x - x' > 0$ is based on the principle that the x-coordinates of the minutiae from the left-view image must be larger than those of corresponding minutiae from the right-view image (see Fig. 1). The constraint term $|y - y'| < \sigma_y$ is based on the fact that the corresponding minutiae are located in the same or adjacent rows in the rectified ridge maps. Thus, the benchmark pair of minutiae is selected from all the candidate ones that satisfy these constraints using the transformation-based method in [1], [26]. To enhance robustness, if a selected benchmark minutia is a bifurcation one, we replace it with its corresponding ending minutia. The curves where the benchmark pair of minutiae is located is defined as benchmark curves.

The proposed dynamic algorithm used to calculate the RVCM M based on the benchmark curves consists of: a benchmark curves-based calculation stage (BS); and a dynamic updating stage (DS) (see the supplementary material, which can be found on the Computer Society Digital Library at http://doi.ieeecomputersociety.org/10.1109/TPAMI.2019.2949299.). For convenience, we denote (x_i, y_i) and (x'_i, y'_i) as the coordinates of the benchmark pair of minutiae $\mathbf{m_i}$ and $\mathbf{m'_i}$, respectively, and L_i and L'_i as the corresponding curve labels in SRVMs $\mathcal{M}$ and $\mathcal{M}'$, respectively. In the following paper, we also refer to L_i and L'_i as the RV curves since each isolated curve is assigned a unique integer value which is used as its label (Section 2.2).

The BS calculates M along the benchmark curves L_i and L'_i row by row and the DS dynamically updates M according to the remaining rows in $\mathcal{M}$ and $\mathcal{M}'$, with the *Row-Operator* for calculating M for each row illustrated in Fig. 3. $\mathbf{R} = \{\ldots, L_{r2}, L_{v2}, L_{r1}, L_{v1}, L_s, \ldots\}$ and $\mathbf{R}' = \{\ldots, L'_{r2}, L'_{v2}, L'_{r1}, L'_{v1}, L'_s, \cdots\}$ are denoted as the salient label vectors for the same row in $\mathcal{M}$ and $\mathcal{M}'$, respectively, which are generated by removing adjacent labels with the same value. This ensures that the values of a salient label vector alternately represent ridges and valleys, thereby enabling the *Row-Operator* to efficiently determine the correspondence between their curves. The *Row-Operator* calculates the values of M from the matched labels L_s and L'_s, first backwards to the first pair of labels and then forwards to the last pair by $e_{ij} = e_{ij} + 1$, where i and j are the matched curve labels. In BS, the matched labels L_s and L'_s are the labels of the benchmark curves and, in DS, are dynamically determined by the maximum value of the current row in M. With $\tilde{y_a}$ and $\tilde{y_b}$ denoted as the minimum and maximum row indexes of the curves, respectively, the calculation ranges of BS and DS are $(\tilde{y_a}, \tilde{y_b})$, and $(0, \tilde{y_a} - 1)$ and $(\tilde{y_b} + 1, n)$, respectively.

2.3.3 Establishment of RVC

We establish a RVC $\mathcal{C} \stackrel{def}{=} \langle \tilde{\mathcal{M}}, \tilde{\mathcal{M}}' \rangle$ by updating the SRVMs $\mathcal{M}$ and $\mathcal{M}'$ based on the RVCM M. According to the definition of a RVCM

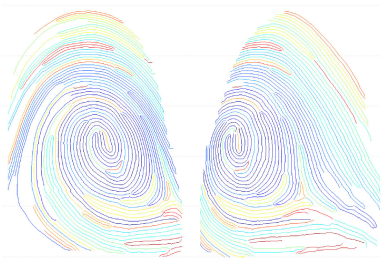

Fig. 4. Result for RVC, where corresponding RV curves have same color.

(Section 2.3.1), a larger value of element e_{ij} indicates a better correspondence between curves i and j. Therefore, curves i and j from $\mathcal{M}$ and $\mathcal{M}'$, respectively, are considered a match if e_{ij} is the largest value in row i or column j of M. This operation enhances the error tolerance of the established RVC to the SRVMs. A greedy algorithm is developed for this purpose (see the supplementary material, available online). Fig. 4 shows a RVC result established using the proposed algorithm.

2.4 Reconstruction of 3D Depth Information

3D depth information is calculated based on the disparity map which, traditionally, is calculated at the pixel level. To improve robustness, we calculate a RDP at the curve level, which fully considers the unique characteristics of the RV structure of a 3D fingerprint.

The proposed RDP calculation consists of three steps: 1) RV disparity computation; 2) RV disparity refinement; and 3) RDP interpolation. In the first step, the disparities of the points located on the RV curves are calculated. Since their corresponding curves are assigned the same value in $\mathcal{C}$, it is easy to obtain the corresponding points ((x, y) in $\tilde{\mathcal{M}}$ and (x', y) in $\tilde{\mathcal{M}}'$) and calculate their disparity $d(x, y)$ using Eq. (2). In the second step, smoothing is performed to refine the RV disparity and suppress spike-like noise. Since traditional smoothing methods conducted in 2D space tend to damage a RV's depth structure, we propose a curve-based one undertaken in 1D space to preserve this structure in local regions. First, a disparity vector is generated by extracting the disparities of each point in a RV curve along the curve's direction. Then, median and average filtering are conducted sequentially on the disparity vector to achieve curve-based smoothing on all curves in $\tilde{\mathcal{M}}$ which refines the RV disparity. Fig. 5 illustrates this process for one curve. In the third step, the disparities of the points between ridges and valleys are quickly interpolated based on the refined RV disparity to obtain the RDP for the whole fingerprint.

After obtaining the RDP, 3D fingerprint reconstruction is achieved using Eq. (1). Fig. 6 comprehensively shows the results obtained from this method for one finger which demonstrate the successful recovery of 3D RVs and generation of well-structured 3D surfaces. Fig. 7 shows the results for a contaminated finger, demonstrating the performance of the proposed method in tough cases.

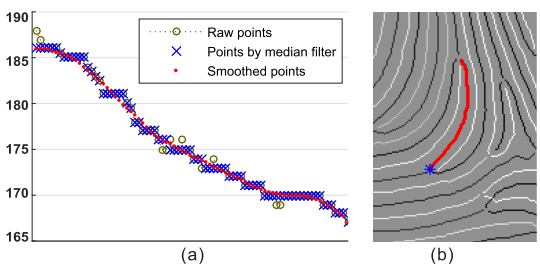

Fig. 5. Diagram of proposed curve-based smoothing. (a) Disparity vectors of example curve highlighted in red in (b), where gray circles represent initially calculated disparities, blue crosses disparities after median filtering, and red points disparities after average filtering.

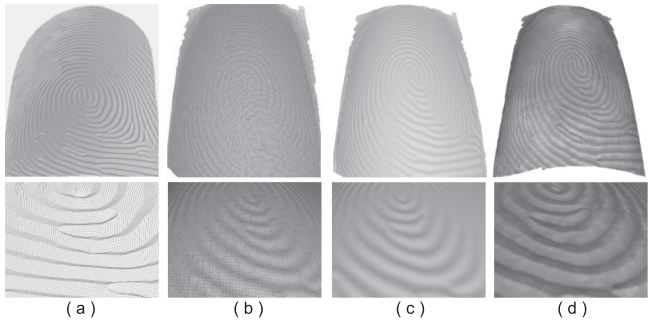

Fig. 6. 3D reconstruction results of our method for one finger: (a) 3D point cloud; (b) the mesh; (c) 3D surface; and (d) textured 3D surface.

3 TTP Feature Extraction

For highly accurate 3D fingerprint recognition, first, 3D minutiae are extracted and re-represented in new 3D spaces with each minutia being the new origin (Section 3.1) and then a TTP feature of a 3D fingerprint, which fully exploits the 3D topological information of its 3D minutiae, is extracted(Section 3.2).

3.1 Extraction and Re-Representation of 3D Minutiae

As a 3D minutia is a nature extension of a 2D minutia in 3D space, we represent it by a quintuplet $\{x, y, z, \theta, \phi\}$, where x, y, z are the coordinates with z representing the depth, and θ and ϕ the minutia's directions representing the 3D ridge orientation. In our work, first, 2D minutiae are extracted using the software VeriFinger [40] and then the 3D ones are obtained by calculating ϕ from the 3D cloud points using the method in [41]. Denoting $\mathbf{M^{3D}} = \{\mathbf{m_1^{3D}}, \mathbf{m_2^{3D}}, \ldots, \mathbf{m_m^{3D}}\}$ as the set of 3D minutiae of a 3D fingerprint, for each one, e.g., $\mathbf{m_i^{3D}} = \{x_i, y_i, z_i, \theta_i, \phi_i\}$ in $\mathbf{M^{3D}}$, we use it as an origin to create a new 3D coordinate system $\mathcal{S}_i$ and re-represent the remaining ones in this new 3D space. This operation, which can be intuitively understood as rotating a 3D fingerprint around the current minutia with angles of θ_i and ϕ_i to simulate human observations of a 3D fingerprint from multiple perspectives, provides the basis for the following TTP feature extraction.

For a concise presentation in this section, the 3D minutia set $\mathbf{M^{3D}}$ and 3D minutia $\mathbf{m_i^{3D}}$ are hereafter simply denoted as $\mathbf{M}$ and $\mathbf{m_i}$ which does not introduce any ambiguity as only 3D minutiae are involved.

Creating a new 3D coordinate system $\mathcal{S}_i$ with minutia $\mathbf{m_i} = \{x_i, y_i, z_i, \theta_i, \phi_i\}$ as the origin means setting the new representation $\mathbf{m_i'} = \{x_i', y_i', z_i', \theta_i', \phi_i'\}$ of $\mathbf{m_i}$ as $(0, 0, 0, 0, 0)$. Therefore, the new representation $\mathbf{m_j'} = \{x_j', y_j', z_j', \theta_j', \phi_j'\}$ of the remaining minutia $\mathbf{m_j} = \{x_j, y_j, z_j, \theta_j, \phi_j\}$ in $\mathbf{M}$ can be calculated by

$$\begin{bmatrix} x_j' \\ y_j' \\ z_j' \end{bmatrix} = T_y(-\phi_i) T_z(-\theta_i) \begin{bmatrix} x_j - x_i \\ y_j - y_i \\ z_j - z_i \end{bmatrix}, \tag{3}$$

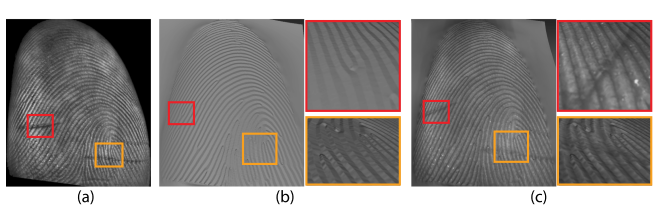

Fig. 7. 3D reconstruction results for (a) a contaminated finger, (b) 3D surface, and (c) textured 3D surface are both reconstructed with the contaminated pattern being removed.

TABLE 1
Comparison of 3D Fingerprint Reconstruction Time of State-of-the-Art Methods

Categories	Methods	Time (/points)	Size/Cost	RV Details
Photometric Stereo	Xie et al. [4]	180s/60K	small/low	yes
	Kumar et al. [5]	7.5s/2.8M		
	Lin et al. [6]	3s/1.2M		
Structured Light	Wang et al. [7]	1s/5M	bulky/high	yes
	Huang et al. [8]	0.5s/450K		
Stereo Vision	Parziale et al. [11]	very long	med./med.	no
	Liu et al. [12]	90s/45K	small/low	
	Labati et al. [13]	24s/1.2M		
	Our Method	**0.1s/1.2M**	**small/low**	**yes**

and

$$\left[1, \theta'_j, \phi'_j\right]^T = Tr(T_y(-\phi_i)T_z(-\theta_i)Tr^{-1}(1, \theta_j, \phi_j)), \tag{4}$$

where function $T_y(\phi)$ is formulated as

$$T_y(\phi) = \begin{bmatrix} \cos\phi & 0 & -\sin\phi \\ 0 & 1 & 0 \\ \sin\phi & 0 & \cos\phi \end{bmatrix}, \tag{5}$$

function $T_z(\theta)$ as

$$T_z(\theta) = \begin{bmatrix} \cos\theta & -\sin\theta & 0 \\ \sin\theta & \cos\theta & 0 \\ 0 & 0 & 1 \end{bmatrix}, \tag{6}$$

function $Tr(u, v, w)$, which is the transformation from a Cartesian to spherical coordinate system, as

$$Tr(x, y, z) = \begin{bmatrix} 1 \\ \arctan 2(y, x) \\ \arcsin(z/\sqrt{x^2 + y^2 + z^2}) \end{bmatrix}, \tag{7}$$

and function $Tr^{-1}(1, \theta, \phi)$, which is the inverse transform of $Tr(x, y, z)$, as

$$Tr^{-1}(1, \theta, \phi) = [\cos\theta\cos\phi, \sin\theta\cos\phi, \sin\phi]^T. \tag{8}$$

By performing this for every minutia, m 3D spaces $\{\mathcal{S}_1, \cdot, \mathcal{S}_m\}$ and m new representations $\{\mathbf{M}'_1, \cdot, \mathbf{M}'_m\}$ of the set of minutiae $\mathbf{M}$ are obtained.

3.2 Extraction and Recognition of TTP Feature

The TTP feature is extracted by coding the 2D topologies of the set of 3D minutiae on multiple planes determined by the multiple 3D spaces created in Section 3.1. Denote $\mathbf{M}'_\mathbf{i} = \{\mathbf{m}'_\mathbf{1}, \mathbf{m}'_\mathbf{2}, \cdots, \mathbf{m}'_\mathbf{m}\}$ as the set of 3D minutiae represented in $\mathcal{S}_i$ with $\mathbf{m}'_\mathbf{i}$ as the origin. First, a 2D minutia set $\mathbf{M}''_\mathbf{i} = \{\mathbf{m}''_\mathbf{1}, \mathbf{m}''_\mathbf{2}, \ldots, \mathbf{m}''_\mathbf{m}\}$ centered at $\mathbf{m}'_\mathbf{i}$ is generated by projecting $\mathbf{M}'_\mathbf{i}$ onto the xy-plane of $\mathcal{S}_i$. Then, the local topology $\mathcal{T}_i$ of $\mathbf{M}''_\mathbf{i}$, which can be considered the projection of the topology of $\mathbf{M}'_\mathbf{i}$ and further understood as the depiction of the topology of $\mathbf{M}$ in $\mathcal{S}_i$, is extracted by calculating the MCC [30] of $\mathbf{m}''_\mathbf{i}$ on $\mathbf{M}''_\mathbf{i}$. Finally, the m topologies corresponding to m re-represented minutia sets in m 3D spaces are obtained and coded as the TTP $\mathcal{T} = \{\mathcal{T}_i, \mathcal{T}_2, \ldots, \mathcal{T}_m\}$ to represent a 3D fingerprint.

The effectiveness of the proposed TTP feature can be justified by the following facts. Two sets of 3D minutiae of the same finger should have the similar 3D minutiae topology including their relative orientation relationship, which should be invariant to the rotation and shift of the finger. Therefore, their 2D projections based on the same registered minutia should preserve the same 2D minutiae topology including their relative orientation relationships. Apparently, such 2D projections involve the 3D topology of the relevant 3D minutiae including their 3D minutiae relationships. Since this extraction considers only the spaces determined by the 3D minutiae and the topology for the origin minutia, it is particularity efficient. Also, by reducing its dimension from 3D to 2D, this TTP feature extraction significantly reduces computational complexity: for example, the running time for a minutia set $\mathbf{M}$ containing 200 3D minutiae is approximately 7ms. After this TTP extraction, 3D fingerprint recognition is achieved by calculating the comparison score of two TTP features using the LSA-R method [30].

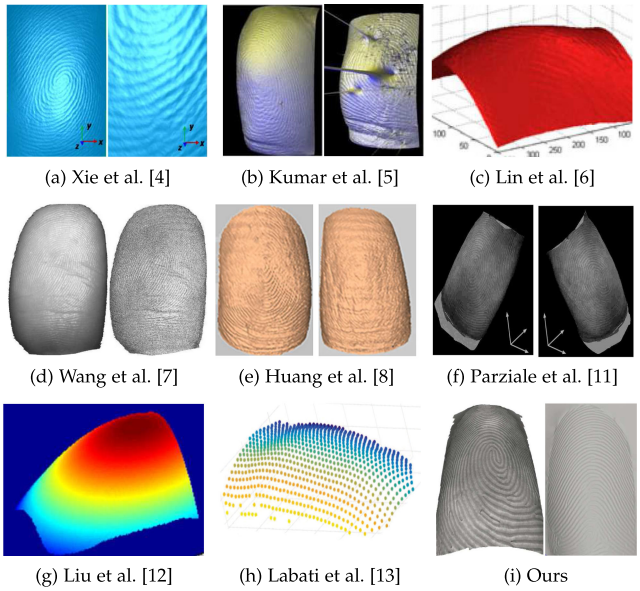

(a) Xie et al. [4] (b) Kumar et al. [5] (c) Lin et al. [6]
(d) Wang et al. [7] (e) Huang et al. [8] (f) Parziale et al. [11]
(g) Liu et al. [12] (h) Labati et al. [13] (i) Ours

Fig. 8. Comparison of 3D fingerprint surface reconstructed using the methods based on photometric stereo ((a), (b), and (c)), structured light ((d) and (e)), and stereo vision ((f), (g), (h), and (i)).

4 Experimental Results and Discussion

We evaluate the performance of our method in terms of both reconstructing and recognizing 3D fingerprints.

4.1 3D Fingerprint Reconstruction

The performance of our 3D fingerprint reconstruction method is compared with those of eight state-of-the-art ones, with their reconstruction times and levels of accuracy.

4.1.1 Reconstruction Time

Running time is critical for a 3D AFRS in practical applications. Table 1 presents the times taken by the different methods and their corresponding requirements and outputs, with those in bold the best. As can be seen, our method achieves an outstanding performance as it takes approximately 0.1 seconds to reconstruct a 3D fingerprint with 1.2 million points, that is, real-time 3D fingerprint reconstruction. In comparison with the other methods, it can be concluded that ours is approximately 2.5 and 10 times faster than the second and third fastest method in Ref. [7] and [8], respectively.

4.1.2 Accuracy of Reconstruction

The performance of our 3D fingerprint reconstruction method can be verified by visually inspecting the results provided in Figs. 6 and 7. It is clear that, for all the regions, including the minutia and contaminated ones, our method provides good subjective visual quality with a well-reconstructed RV structure. Moreover, the entire reconstructed 3D fingerprint is spotless and noise-free. For better evaluation, some 3D reconstruction results obtained by

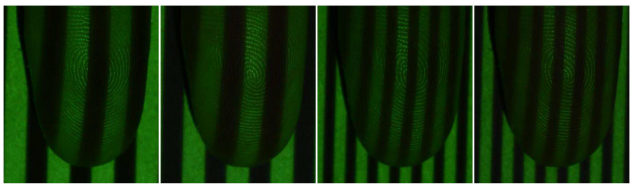

Fig. 9. Fingerprints with illuminated patterns.

our and eight other methods are shown in Fig. 8. It can be seen that the results of the method in [5] are anomalous and even have spike-like noise, those of the method in [7] are very noisy, and those of the method in [8] have lots of weird strip shadows that are obviously not the fingerprint textures. The results of traditional stereo vision-based methods in [11], [12], [13] tend to be smooth surfaces without RV structure. The inability of these methods to recover RV depth information is due mainly to their establishment of correspondence being based on region blocks whereas our method overcomes this problem and achieves highly accurate 3D fingerprint reconstruction results.

To quantitatively evaluate the performance of our reconstruction method, we adopt two metrics of percentage of bad matching pixels (PBP) and root-mean-squared (RMS) error to estimate the reconstruction accuracy as in [42], [43]. The ground-truth 3D fingerprint is obtained using a structured light illumination method in [42], with two Nikon D750 cameras and a DLP LightCrafter Display 3010 evaluation module Gen2 from Texas Instruments synchronized through a program developed on the open source software digiCamControl [44] and Psychtoolbox [45]. In the experiment, sixty ground-truth samples are obtained for twenty fingers, with three samples for each finger. Fig. 9 shows some collected fingerprints with illuminated patterns. Fig. 10 shows samples of a ground-truth disparity map and a reconstructed one from our method, with the average PBPs for different error thresholds provided. The average RMS errors for dense, ridge, and valley disparities are approximately 3.37, 3.26, and 3.22, respectively.

4.2 3D Fingerprint Recognition

Comprehensive experiments are conducted on two databases to evaluate and compare the 3D fingerprint recognition performances of our proposed and state-of-the-art methods in terms of both recognition accuracy and running time. DB1 is a 3D fingerprint database generated by our reconstruction method with stereo fingerprint images obtained from a three-camera system, containing 3000 3D fingerprints from 1500 different fingers. DB2 [5] is a publicly available 3D fingerprint database consisting of 1400 3D fingerprints from 240 different fingers. Therefore, DB1 has 1500 genuine and 1,124,250 ($1500 \times 1449/2$) impostor comparisons, respectively, and DB2 has 3600 ($240 \times 6 \times 5/2$) genuine and 28,680 ($240 \times 239/2$) impostor comparisons, respectively. All the experiments are implemented in C\C++ and run on a workstation with Intel Xeon E5-2670 CPUs powered by a Linux system.

Table 2 shows the 3D fingerprint recognition performances of our and three methods in [5], [6], [13] evaluated on DB1 and DB2 with respect to their EER and rank-1 accuracy values and average times,

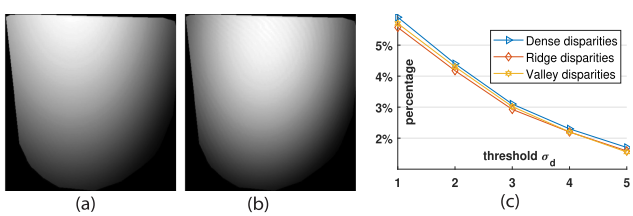

Fig. 10. Samples of (a) ground-truth disparity map and (b) reconstructed one from our method, with (c) the average PBPs for different thresholds.

TABLE 2
Comparison of Performances for 3D Fingerprint Recognition of State-of-the-Art Methods Evaluated on Databases DB1 and DB2

Methods	Equal Error Rate(%)			Rank-1 Accuracy(%)			Avg. Time
	DB1	DB2	Avg.	DB1	DB2	Avg.	
FR1 [5]	0.96	1.02	0.99	98.1	96.7	97.4	2.435s
FR2 [13]	**0.62**	0.70	**0.66**	97.3	96.5	96.9	5.670s
FR3 [6]	1.39	1.51	1.45	98.2	**97.7**	97.95	0.380s
Our	0.64	**0.68**	**0.66**	**98.5**	97.6	**98.05**	**0.046s**
VM	2.08	1.47	1.78	97.1	95.8	96.45	0.031s
VU	1.39	1.51	1.45	97.8	97.1	97.45	0.036s

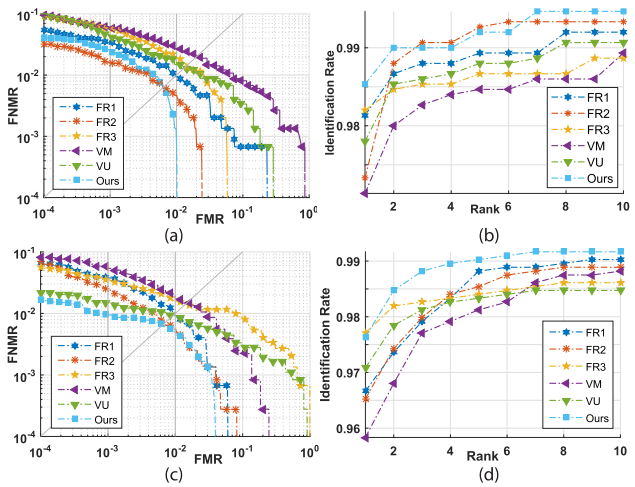

Fig. 11. Comparison of ROC and CMC curves for 3D fingerprint recognition of state-of-the-art methods evaluated on databases DB1 and DB2.

with those in bold the best, and the performances of VM (multi-view 2D fingerprints recognition using Verifinger 6.3 [40]) and VU (unwrapped 3D fingerprints [7] recognition using Verifinger 6.3). It is clear that our method achieves the highest rank-1 accuracy on DB1, the lowest EER on DB2, and the best average EER and average rank-1 accuracy, with the shortest average comparison time. For a comprehensive evaluation, ROC and CMC curves of our and the three methods performed on DB1 and DB2 are shown in Fig. 11, with those of the VM and VU methods the benchmarks.

5 Conclusion

We proposed a robust 3D AFRS based on RV-guided 3D reconstruction and TTP feature extraction. The former establishes RVCs based on the topology of RV curves, which is different from traditional methods that establish correspondences between points and considers the unique fingerprint characteristics of the RV so that achieves real-time reconstruction. The latter extracts the TTP feature which codes the 3D topology by projecting the 3D minutiae onto multiple planes and extracting their corresponding 2D topologies and has proven to be effective and efficient for 3D fingerprint recognition. The comprehensive experimental results demonstrate that the proposed method outperforms state-of-the-art ones in terms of both the reconstruction and recognition of a 3D fingerprint and, due to its significantly short running time, is suitable for practical applications.

Despite this method's promising results, more research can be conducted to improve the reliability of a 3D AFRS. In the future, potential anti-spoofing capability for enhancing the security of biometrics systems could be studies as 3D fingerprints provide the real 3D space information of fingers.

ACKNOWLEDGMENTS

This research is supported by ARC Discovery Grant (ID DP190103660) and ARC Linkage Grant (ID LP180100663).

REFERENCES

[1] D. Maltoni, D. Maio, A. K. Jain, and S. Prabhakar, *Handbook of Fingerprint Recognition*, 2nd ed. Berlin, Germany: Springer, 2009.
[2] S. M. Furman, B. C. Stanton, M. F. Theofanos, J. M. Libert, and J. D. Grantham, "Contactless fingerprint devices usability test," National Inst. Standards Technol., Gaithersburg, MD, Tech. Rep. 8171, 2017.
[3] X. Pang, Z. Song, and W. Xie, "Extracting valley-ridge lines from point-cloud-based 3D fingerprint models," *IEEE Comput. Graphics Appl.*, vol. 33, no. 4, pp. 73–81, Jul./Aug. 2013.
[4] W. Xie, Z. Song, and R. C. Chung, "Real-time three-dimensional fingerprint acquisition via a new photometric stereo means," *Optical Eng.*, vol. 52, 2013, Art. no. 103103.
[5] A. Kumar and C. Kwong, "Towards contactless, low-cost and accurate 3D fingerprint identification," *IEEE Trans. Pattern Anal. Mach. Intell.*, vol. 37, no. 3, pp. 681–696, Mar. 2015.
[6] C. Lin and A. Kumar, "Tetrahedron based fast 3D fingerprint identification using colored LEDs illumination," *IEEE Trans. Pattern Anal. Mach. Intell.*, vol. 40, no. 12, pp. 3022–3033, Dec. 2018.
[7] Y. Wang, L. G. Hassebrook, and D. L. Lau, "Data acquisition and processing of 3-D fingerprints," *IEEE Trans. Inf. Forensics Security*, vol. 5, pp. 750–760, 2010.
[8] S. Huang et al., "3D fingerprint imaging system based on full-field fringe projection profilometry," *Optics Lasers Eng.*, vol. 52, pp. 123–130, 2014.
[9] S. Rusinkiewicz, O. Hall-Holt, and M. Levoy, "Real-time 3D model acquisition," vol. 21, pp. 438–446, 2002.
[10] V. G. Yalla and L. G. Hassebrook, "Very high resolution 3D surface scanning using multi-frequency phase measuring profilometry," *Spaceborne Sensors II*, vol. 5798, pp. 44–54, 2005.
[11] G. Parziale, E. Diaz-Santana, and R. Hauke, "The surround imager: A multi-camera touchless device to acquire 3D rolled-equivalent fingerprints," in *Proc. Int. Conf. Biometrics*, 2006, pp. 244–250.
[12] F. Liu and D. Zhang, "3D fingerprint reconstruction system using feature correspondences and prior estimated finger model," *Pattern Recognit.*, vol. 47, pp. 178–193, 2014.
[13] R. D. Labati, A. Genovese, V. Piuri, and F. Scotti, "Toward unconstrained fingerprint recognition: A fully touchless 3-D system based on two views on the move," *IEEE Trans. Syst. Man Cybern. Syst.*, vol. 46, no. 2, pp. 202–219, Feb. 2016.
[14] R. J. Woodham, "Photometric method for determining surface orientation from multiple images," *Optical Eng.*, vol. 19, 1980, Art. no. 191139.
[15] C. Sousedik, R. Breithaupt, and C. Busch, "Volumetric fingerprint data analysis using optical coherence tomography," in *Proc. Int. Conf. BIOSIG Special Interest Group*, 2013, pp. 1–6.
[16] E. Auksorius and A. C. Boccara, "Fast subsurface fingerprint imaging with full-field optical coherence tomography system equipped with a silicon camera," *J. Biomed. Opt.*, vol. 22, 2017, Art. no. 096002.
[17] Y. Cheng and K. V. Larin, "Artificial fingerprint recognition by using optical coherence tomography with autocorrelation analysis," *Appl. Opt.*, vol. 45, pp. 9238–9245, 2006.
[18] P. Hariharan, *Basics of Interferometry*. Amsterdam, The Netherlands: Elsevier, 2010.
[19] S. Kim, M. Crose, W. J. Eldridge, B. Cox, W. J. Brown, and A. Wax, "Design and implementation of a low-cost, portable oct system," *Biomed. Opt. Express*, vol. 9, pp. 1232–1243, 2018.
[20] H. Tang et al., "3D ultrasonic fingerprint sensor-on-a-chip," *IEEE J. Solid-State Circuits*, vol. 51, no. 11, pp. 2522–2533, Nov. 2016.
[21] X. Jiang et al., "Monolithic ultrasound fingerprint sensor," *Microsystems Nanoengineering*, vol. 3, 2017, Art. no. 17059.
[22] R. G. Maev and F. Severin, "High-speed biometrics ultrasonic system for 3D fingerprint imaging," in *Proc. Opt. Photonics Counterterrorism Crime Fighting Defence VIII*, vol. 8546, pp. 85–90, 2012.
[23] F. Liu, D. Zhang, and L. L. Shen, "Study on novel curvature features for 3D fingerprint recognition," *Neurocomputing*, vol. 168, pp. 599–608, 2015.
[24] T.-P. Fang and L. A. Piegl, "Delaunay triangulation in three dimensions," *IEEE Comput. Graphics Appl.*, vol. 15, pp. 62–69, Sep. 1995.
[25] W. Yang, J. Hu, and S. Wang, "A delaunay quadrangle-based fingerprint authentication system with template protection using topology code for local registration and security enhancement," *IEEE Trans. Inf. Forensics Security*, vol. 9, pp. 1179–1192, Jul. 2014.
[26] X. Jiang and W. Y. Yau, "Fingerprint minutiae matching based on the local and global structures," in *Proc. Int. Conf. Pattern Recognit.*, 2000, vol. 2, pp. 1038–1041.
[27] N. K. Ratha, R. M. Bolle, V. D. Pandit, and V. Vaish, "Robust fingerprint authentication using local structural similarity," *Proc. IEEE Workshop Appl. Comput. Vis.*, 2000, pp. 29–34.
[28] J. Feng, "Combining minutiae descriptors for fingerprint matching," *Pattern Recognit.*, vol. 41, pp. 342–352, 2008.
[29] M. Tico and P. Kuosmanen, "Fingerprint matching using an orientation-based minutia descriptor," *IEEE Trans. Pattern Anal. Mach. Intell.*, vol. 25, no. 8, pp. 1009–1014, Aug. 2003.
[30] R. Cappelli, M. Ferrara, and D. Maltoni, "Minutia cylinder-code: A new representation and matching technique for fingerprint recognition," *IEEE Trans. Pattern Anal. Mach. Intell.*, vol. 32, no. 12, pp. 2128–2141, Dec. 2010.
[31] D. Peralta et al., "A survey on fingerprint minutiae-based local matching for verification and identification: taxonomy and experimental evaluation," *Inf. Sci.*, vol. 315, pp. 67–87, 2015.
[32] R. Hartley and A. Zisserman, *Multiple View Geometry in Computer Vision*, 2nd ed. Cambridge, U.K.: Cambridge Univ. Press, 2003.
[33] Z. Zhengyou, "A flexible new technique for camera calibration," *IEEE Trans. Pattern Anal. Mach. Intell.*, vol. 22, no. 11, pp. 1330–1334, Nov. 2000.
[34] J. Heikkila and O. Silven, "A four-step camera calibration procedure with implicit image correction," in *Proc. IEEE Comput. Society Conf. Comput. Vis. Pattern Recognit.*, 1997, pp. 1106–1112.
[35] B. Li, L. Heng, K. Koser, and M. Pollefeys, "A multiple-camera system calibration toolbox using a feature descriptor-based calibration pattern," in *Proc. IEEE/RSJ Int. Conf. Intell. Robots Syst.*, 2013, pp. 1301–1307.
[36] K. K. Bo Li, Lionel Heng, and M. Pollefeys. Multiple camera calibration toolbox. Nov. 3, 2013. [Online]. Available: https://sites.google.com/site/prclibo/toolbox
[37] J.-Y. Bouguet. Camera calibration toolbox for matlab. Dec. 4, 2003. [Online]. Available: http://www.vision.caltech.edu/bouguetj/index.html
[38] Y. Zhu, X. Yin, X. Jia, and J. Hu, "Latent fingerprint segmentation based on convolutional neural networks," in *Proc. IEEE Workshop Inf. Forensics Security*, 2017, pp. 1–6.
[39] S. Chikkerur, A. N. Cartwright, and V. Govindaraju, "Fingerprint enhancement using STFT analysis," *Pattern Recognit.*, vol. 40, pp. 198–211, 2007.
[40] Neurotechnology verifinger SDK. June 2011. [Online]. Available: http://www.neurotechnology.com/ verifinger.html
[41] J.-F. Lalonde, N. Vandapel, and M. Hebert, "Automatic three-dimensional point cloud processing for forest inventory," Carnegie Mellon Univ., Pittsburgh, PA, Tech. Rep. CMU-RI-TR-06–21, 2006.
[42] D. Scharstein and R. Szeliski, "High-accuracy stereo depth maps using structured light," in *Proc. IEEE Comput. Society Conf. Comput. Vis. Pattern Recognit.*, 2003, vol. 1, pp. 195–202.
[43] D. Scharstein and R. Szeliski, "A taxonomy and evaluation of dense two-frame stereo correspondence algorithms," *Int. J. Comput. Vis.*, vol. 47, pp. 7–42, 2002.
[44] digiCamControl. May 6, 2013. [Online]. Available: http://digicamcontrol.com/
[45] Psychtoolbox. Jan. 1, 1997. [Online]. Available: http://psychtoolbox.org/